Assessment of agglomerated ceramic powders under impact by cold spraying

Geoffrey Celeste, Vincent Guipont, Djamel Missoum-Benziane, Guillaume Kermouche, Sergio Sao-Joao, Séverine Girard- Insardi, Dylan Chatelain

Assessment of agglomerated ceramic powders under impact by cold spraying

G. CELESTE[1], V. GUIPONT[1], D. MISSOUM-BENZIANE[1], G. KERMOUCHE[2], S. SAO-JOAO[2], S. GIRARD-INSARDI[2], D. CHATELAIN[3]

[1] Centre des matériaux – CMAT, Mines Paris-PSL, UMR CNRS 7633 ; 63-65 rue Henri-Auguste Desbruères, 91000 EVRY, France
[2] Mines Saint-Etienne, Univ Lyon, CNRS, UMR 5307 LGF, Centre SMS, F - 42023 Saint-Etienne, France
[3] Institut de Recherche sur les Céramiques (IRCer), UMR CNRS 7315 ; 12 rue Atlantis, 87068 LIMOGES, France

Abstract

Most of ductile metals can be deposited by cold spray (CS). For brittle ceramic, such solid-state deposition process is still questionable, but some recent work on $Ti0_2$ or hydroxyapatite powders have shown that micrometric ceramic powder could be deposited by CS. In this work, it is claimed that the nature and the porous architecture of a ceramic powder with agglomerated ultra-fine grains play an important role on the impact behaviour. The aim of this work is to investigate the deformation behaviour of ceramic agglomerated powders under high velocity impact. Two different powders, respectively 3YSZ and Y_2O_3, were selected in order to study their architectures (particle size, porosity, density, crystallite size, etc.). Cold spray "splats" experiments, with various spraying distances to vary the particles velocities upon impact, were carried out to observe the deformation and fragmentation. In case of Y_2O_3, cold spray with dynamic vacuum surrounding atmosphere up to 3kPa were also prepared to evaluate the role of the atmosphere on the resulting impact. In parallel, in situ SEM micro-compression tests at 10^{-2} s^{-1} on cross-sectioned 3YSZ particles involving flat-punch nano-indentation and micropillar compression were performed. By modelling the compression tests, the aim is to identify a Drücker-Prager behaviour law suitable for an agglomerated ceramic powder under quasi-static compression. Such deformation behaviour could help to better understand the compaction behaviour of agglomerated powders.

1. Introduction

Cold Spray (CS) is a solid-state deposition process based on severe plastic deformation of powders. It is well established that ductile metallic materials can be processed by cold spray for coating solutions, repairing or manufacturing applications [1], [2] With such spraying process, rather fine powders (20-50 µm) are accelerated by a supersonic gas stream at a temperature lower than the melting temperature of the material. Therefore, heat-induced oxidation and phase transformation, thermal stress, and other common problems encountered in thermal spray processes are very limited. Dense coatings involving several pure metals and alloys can be obtained by CS. As-sprayed or heat-treated coatings can exhibit high level mechanical or electrical properties [3], [4].

For brittle ceramics, such "cold" deposition process is still questionable, but it was found that rather thick and adhesive coatings could be obtained with specific ceramic powders deposited on metallic, ceramic, or polymeric substrates: e.g., hydroxyapatite (HA) [5]–[7], TiO_2 [8]–[10] Y_20_3 [11] or SiC [12]. Dense ceramic powder is not relevant because the breaking of the particles leads to blocky fragments embedded like grit residues in a sand blasted surface. Recent works on pure ceramics by CS are mainly devoted to ceramic powders in the form of agglomerates that could be more suitable for cold spray deposition. On a fine scale, the nature and size of the crystallites may allow for rearrangements of the material, or even micro-plasticity under the effect of the high energy impact. The impact behaviour of agglomerated powders that can adhere with compaction of the porous particles has been evidenced in case of HA or TiO_2 when powders are exhibiting nano-sized grains [13], [14]. Therefore, the synthesis route can play a role like for TiO_2 anatase powder involving hydrothermal process [15]. Moreover, powder post-treatment like calcination of TiO_2 can have a significant role on the resulting coating build up [16]. The nature and the surface morphology of the substrate could also influence drastically the impact behaviour and the mechanical anchoring of the ceramic powder [17].

For a similar solid-state kinetic spraying of ceramics, known as Aerosol Deposition (AD) process, Akedo et al. introduced the concept of Room Temperature Impact Consolidation (RTIC) [18] and Park et al. suggested a shock-induced plasticity and fragmentation phenomena [19]. In AD, the impact behaviour concerns isolated ultra-fine particles powders previously dispersed in a pressurized gas and further accelerated in a vacuum chamber though a supersonic nozzle. Particles of sufficient size (200nm - 5µm) undergo the RTIC mechanism on impact by fracturing and plastic deformation and therefore adhere to the substrate. [20]. Films and coatings of different natures of ceramics were created: Al_2O_3[21], HA [22], TiO_2 [23], YSZ [24] or Y_2O_3 [25]. For the cold spray of ceramics, the challenge might be to promote the high-velocity impact of such ultra-fine or nano-sized particles when agglomerated in micrometric granules. In addition, it is claimed that the role of the porous architecture of agglomerated particles involving nano-sized and micro-sized features shall have a predominant role on the impact behaviour and the deposition process itself.

The present work aims at exploring the CS of various agglomerated ceramic powders to investigate the role of the nature of the material and those of the architecture of the particles. The purpose is to assess different ceramic materials that could vary with intrinsic toughness and hardness and particles features in the nano-size range (crystallites size, porosity, and internal cohesion). Al_2O_3, ZrO_2 and Y_2O_3 oxide ceramics has been selected because a solid-state deposition process might be of great interested to prevent effects like allotropic, eutectic, amorphous transformations or thermal decomposition that always occur when thermally sprayed. It could also open new processing routes for functional ceramic coatings that could be doped with thermo-sensitive species.

In this work, two nanostructured ceramic feedstock powders: 3YSZ medium, as atomized and Y_2O_3 medium, as atomized from NANOE were prepared by wet method followed by spray drying. The characteristics of each powder were investigated by SEM and physical methods (BET, …) and further "splat" experiments were implemented involving Low Pressure Cold Spray (LPCS) in atmospheric pressure or under dynamic vacuum. The aim is to evaluate the deformation behaviour of individual particles after a dynamic impact in order to address experimentally the mechanisms involved. In parallel, flat punch nano-indentation and micropillar compression experiments were implemented on single 3YSZ particles in order to monitor the mechanical behaviour under micro-compression. By modelling the micro-compression tests, a Drücker-Prager behaviour law suitable for soil materials shall be fitted for agglomerated ceramic according to experimental data of micro-mechanical tests. Future work will focus on this deformation behaviour to be integrated into a numerical particle impact model for comparison with the experimental results of the cold spray.

2. Materials and methods

Ceramic feedstock powders: Two types of agglomerated powders, respectively 3 mol% Yttria Stabilized Zirconia (3YSZ) and cubic Yttria (Y_2O_3), were produced with precursors obtained by wet chemical precipitation (Nanoé, Ballainvilliers, France). After drying, precipitates are dispersed in a liquid suspension. Subsequent atomization of the suspensions was carried out by spray drying. One batch of each atomized ceramic powders, respectively 3YSZ and Y_2O_3 were further prepared by sieving to enable particles diameters ranging between 30-40µm.

Spaying experiments: Aluminium alloy A2017 substrates with 30mm×30mm×3mm dimensions were prepared with one polished surface up to 1µm with a diamond solution and then cleaned with ultrasound. Spraying experiments were carried out using a Low-Pressure Cold Spray facility (LPCS) allowing air or nitrogen gas up to 600°C/0.6MPa (D523, Dycomet Europe, The Netherlands). LPCS system has a radial injection of the powder in the downstream part of the convergent/divergent nozzle. The cold spray gun was installed in a $18m^3$ robotized chamber designed for low pressure plasma spraying. Cold spray parameters involving 0.5MPa of air at 500°C and a corresponding gas flowrate of 18 m^3/h were implemented at atmospheric pressure and also involving dynamic vacuum conditions in order to vary the impact conditions. For these latter, a continuous exhausting of the gaseous atmosphere was managed that corresponded to a measured chamber pressure stabilized at 3kPa during cold spray. Impact conditions were also varied by changing the spraying distances, respectively with 10, 40 and 80mm values. Experiments to collect single isolated particles were implemented with the gun moving at 100mm/s and a 1g/min powder feed rate for both powders. After experiments weakly adhering particles on dusty samples were blown out by applying a gas stream using compressed air nozzle.

Observations and analyses: The flowabilities of the two batches of powders were assessed by Hall Flow method and their humidity rates were measured with humidity scale at 80°C. Thermo-gravimetric analyses (Setaram, Mougins-Sophia Antipolis, France) were implemented to complement the humidity tests. Specific surface area of each powder was measured by BET with nitrogen adsorption (ASAP2000, Micromeritics, USA). Bulk density of the agglomerates was measured by helium pycnometry (AccuPyc II 1340, Micromeritics, USA). X-ray diffraction (XRD) patterns for phase composition analysis were implemented on powders and coatings (D8 Discover,Bruker, USA) with Cu-Kα radiation and a 0–140° 2θ range. The crystallite size of each powder was estimated after Rietveld refinement of diffraction profiles using Le Bail method (Diffrac.Topas software, Bruker, USA).

Mean particle size of each batch of powder was measured by laser particle granulometry (Mastersizer 3000, Malvern Panalytical, Malvern, United Kingdom). Powders (free or cross-sectioned after resin mounting and polishing) and CS splats were observed by Scanning Electron Microscope (Nova NanoSEM 450, FEI, USA) using backscattered electron (BSE) mode. Crushed powders were also imaged by Transmission Electron Microscopy (Tecnaï 20F, FEI, USA) to observe agglomerates of grains. The Vickers micro-hardness of powders was measured on polished cross-section of resin mounted powders (AZ50-4 PRESI, France) with a $0.01kgf/mm^2$ loading force. For these indentation tests, it was ascertained that indent sizes were at least two times smaller than the particle's diameter after cross-section. Thus, 20 indentations on several particles were made for each batch leading to indents diagonals ranging from 17 to 28 µm.

Flat-punch nano-indentation and micropillar compression experiments: Flat punch and micropillar compression tests were developed only on the 3YSZ powder. To that purpose, particles were prepared for in situ SEM nanoindentation experiments and also for micro-compression experiments on FIB-machined micropillars. Resin embedded Y-TZP particles samples of $5x5cm^2$ with a thickness of 0.5cm were prepared using a diamond wire saw followed by polishing with SiC grit papers from P400 to P1200, and then 3µm and 1µm diamond pastes. Micro-

pillars were machined by Focus Ion Beam (FIB) machining using a Thermo Scientific Helios NanoLab DualBeam microscope. First, high beam current (30 kV, 2.5 A) was used to dig a raw pilar shape followed by lower beam current (30 kV, 80 pA) in order to build a sharper and finer geometry of each micropillar. The pillar dimensions shown in Figure 1, are top $D_t = 3.26\mu m$, bottom diameter $D_b = 3.61\ \mu m$ and height $h = 6\ \mu m$. These dimensions will be used for the numerical simulation.

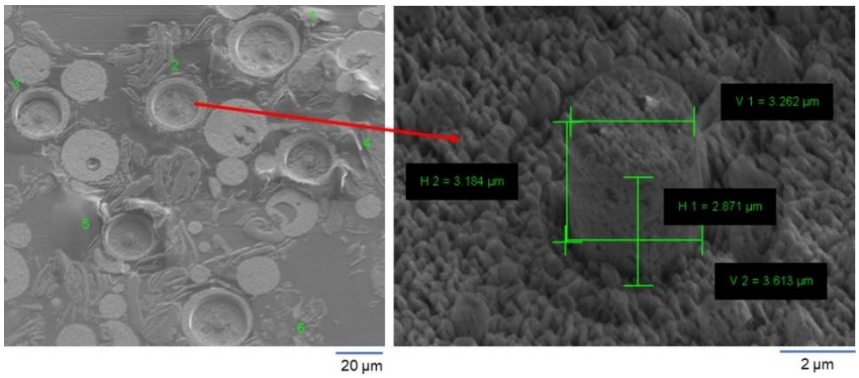

Figure 1. SEM overall and detailed views of FIB-machined micropillars of 3YSZ powder

Micro-compression experiments were achieved using an in-situ SEM indenter (ASA, Alemnis AG, Bern, Switzerland), first developed by Rabe et al. [26]. It is installed in a Zeiss DSM 962 SEM. In situ SEM indentation allows real time monitoring and visualization of material's deformation under tip-loading. The nano-tip is displacement-controlled (piezo actuator) with a feedback loop control. Displacement-controlled devices allow load jumps to be avoided during micro-pilar compression of brittle materials, which can occur during load-controlled tests. A more detailed description of the SEM indenter can be found in [26]. A 25µm diameter flat punch was used for nano-indentation on flat cross-sectioned powder. All the experimental compressions were performed with a tip displacement rate of 100 nm/s. Three micro-compression experiments were achieved on three different micropillars. Two experiments with similar loading conditions and a third one with a series of loading-unloading conditions. The same protocol was implemented for flat punch experiments on three different cross-sectioned particles. With such loading conditions, the maximum in-depth displacements were monitored in the range of 1µm to 4µm. Due to the low displacement rate, series of SEM images were recorded to follow the behaviour of the material during the nano-indentation and micro-compression experiments.

Finite Element Analysis of micro-compression tests: ABAQUS/Standard is implemented to model the flat-punch nano-indentation and micropillar compression experiments. Because of axial symmetry, only half of the sample geometry was meshed using 4-nodes bilinear, hybrid with constant pressure (CAX4H) mesh. Mesh density near the contact surfaces and geometrical singularities was increased. Punch was modelled as full-rigid body with a hard contact boundary condition at the powder/tip interface. Since the DPC model has no rate dependent terms, the FE simulations are considered in a quasi-static loading regime. In actual experiments, as well as in FE simulation, a pillar was dimensioned with top $D_t = 3.26\mu m$, bottom $D_b = 3.61\ \mu m$ diameters and height of $h = 6\ \mu m$. The compression step is modelled by applying a vertical 100 nm/s displacement to the flat punch with a step duration of 15s. Meshed models are shown in Figure 2.

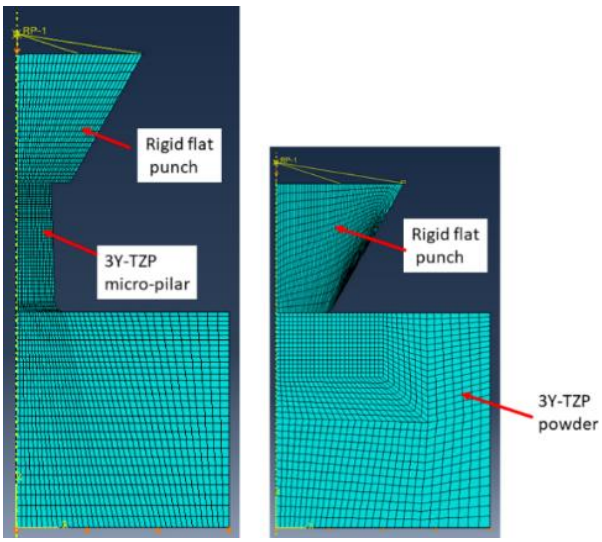

Figure 2. Finite element models for micro-compression tests: micropillar (left), flat punch (right)

Modified Drücker-Prager model: The Drucker-Prager Cap (DPC) model (see Figure 3) is defined in stress space consisting of two coordinates, hydrostatic pressure: $p = \frac{1}{3}(\sigma_{11} + \sigma_{22} + \sigma_{33})$

and Von Mises equivalent stress: $q = \left[\frac{1}{2}(\sigma_{11} - \sigma_{22})^2 + (\sigma_{22} + \sigma_{33})^2 + (\sigma_{33} - \sigma_{11})^2 + 3\sigma_{12}^2 + 3\sigma_{13}^2 + 3\sigma_{23}^2\right]^{\frac{1}{2}}$

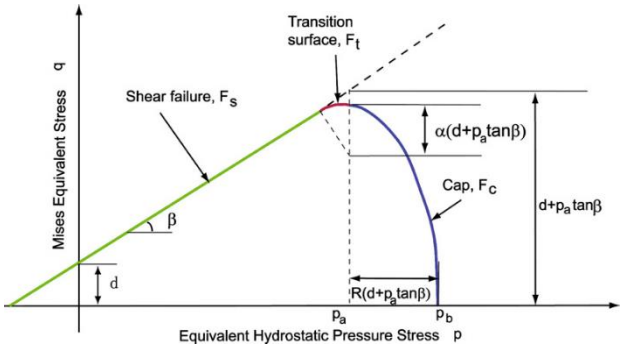

Figure 3. Drucker-Prager Cap model

The yield surface of the model is assumed to be isotropic and includes two main segments, a shear failure surface Fs, and a cap Fc, which intersects the equivalent hydrostatic pressure axis (Figure 3). Within the yield surface the powder is purely elastic. The cap bounds the yield surface in pure hydrostatic compression, providing an inelastic hardening mechanism to represent the plastic nature of compaction. In addition, it controls the volume change, when the material yields by shear. The required softening is provided as a function of inelastic volume increase. To introduce better numerical stability a smooth transition between the two segments, an additional narrow transition region F_t is introduced (modified DPC model) [27].The Drucker–Prager Cap shear failure surface is written as:

$$F_s = q - p\tan\beta - d = 0$$

where β is is the Drucker–Prager Cap friction angle and d describes cohesion. The cap surface is then written as:

$$F_c = \sqrt{(p - p_a)^2 + \left(\frac{Rq}{1+\alpha-\frac{\alpha}{\cos\beta}}\right)^2} - R(d + p_a + \tan\beta) = 0.$$

Here R is a material parameter that controls the shape of the cap, α is a small number used to define the smooth transition surface. p_a is an evolution parameter that represents the volumetric plastic strain driven hardening/softening: $p_a = \frac{p_b - Rd}{1+R\tan\beta}$. The hydrostatic compression yield stress p_b is a function of volumetric plastic strain ε_v^p, which can be expressed as: $\varepsilon_v^p = \ln\frac{\rho}{\rho_0}$ where ρ is the compact relative density and ρ_0 the initial relative density. The transition surface is defined as:

$$F_t = \sqrt{(p - p_a)^2 + \left(q - \left(1 - \frac{\alpha}{\cos\beta}\right)(d + p_a\tan\beta)\right)^2} - \alpha(d + p_a\tan\beta) = 0$$

3. Results and discussions

3.1 Powders analyses

Powders architectures: The powders having already been studied in [Celeste et al., 2021], only results about batches and are reported here. The typical features observed by SEM and TEM are summarized for as atomized and powders in Figure 4. The two agglomerated ceramic powders exhibit particles having a spherical shape and a smooth surface due to the nano-sized and ultra-fine grains. However, some particles have a “donut” morphology which is induced by drying instabilities during atomization. Such defects are not of major concern for a melting process but shall be probably better controlled for a spraying process. Cross-sectioned particles at low and high magnification show the homogeneity and the high compactness of the agglomerated nanostructure. Some micro/nano-pores are present but are difficult to quantify by image analysis and conventional metallography. In case of yttria powder (Figure 4), it is obvious that the architecture is different, much finer than the zirconia powder but exhibiting a rather heterogeneous distribution of nano-sized grains and some coarser agglomerates in the micrometric range. Such architecture led to both nano-sized pores and larger ones. The XRD analyses and the TEM images allow to better estimate the actual size of the grains or crystallites. Two typical morphologies were observed: grains with faceted edges, regular diffraction contrast for 3YSZ and aggregates with more rounded contours, irregular contrast, enclosing nano-pores for Y_2O_3.

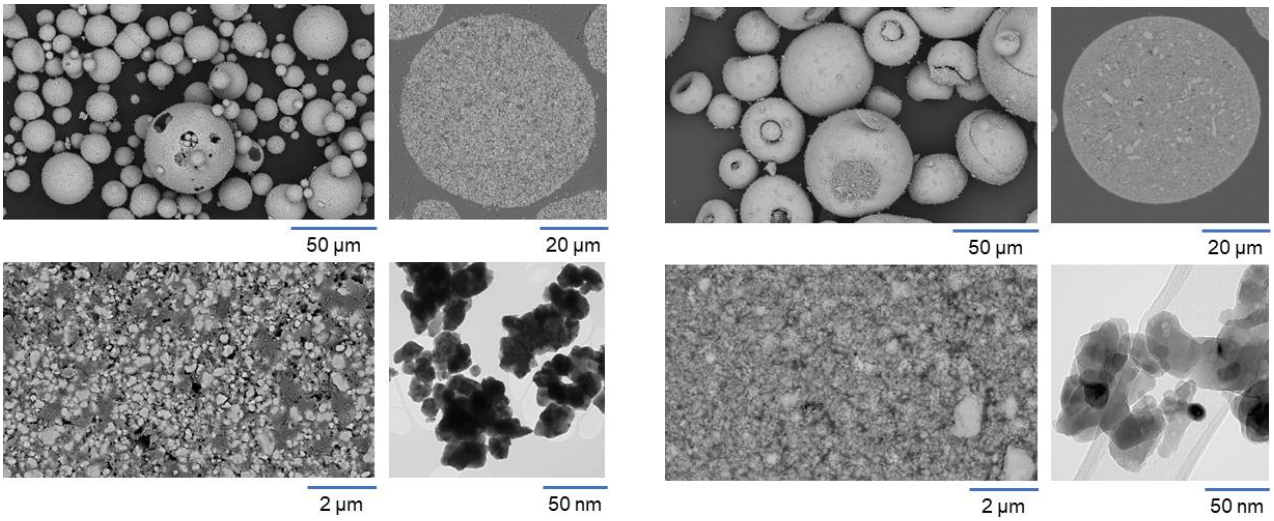

Figure 4. (left) 3YSZ, as atomized; (right) Y_2O_3, as atomized.

Powders characteristics: The two different powders were analysed to investigate structural, physico-chemical, and mechanical characteristics as summarized in Table 1.

Table 1. Powders characteristics

Powder type	ZrO_2	Y_2O_3
Mean diameter, µm	39.9	36.0
Humidity rate, %	0.2	0.39
Hall Flow., s/25g	82	61
He density, g/cm^3	5.94	4.48
Composition, %	43.0 tetragonal 57.0 monoclinic	100.0 cubic
$\rho/\rho_{theoretical}$, %	99,7	89.4
Surface area, m^2/g	10.78	19.8
Crystallite size, nm	79	51
$Hv_{0.1}$	33±6	39±5

Both powders exhibited a similar range of particles size with a mean diameter between 35-40µm. They were both relatively sensitive to humidity therefore pre-heating at 80°C of powders was necessary before and during spraying experiments to improve the powder flowability and prevent detrimental clogging. Phase compositions were analysed by XRD. The as-atomized zirconia powder with yttria addition (3% mol.) was 43.0% tetragonal (t-ZrO_2) and 57.0% monoclinic (m- ZrO_2). Pure yttria powders were cubic (c-Y_2O_3). The corresponding bulk densities measured by He pycnometry were 5.94g/cm^3 for 3YSZ and 4.48g/cm^3 for Y_2O_3. For 3YSZ, the bulk density was only a few percent below the theoretical density but for yttria a higher difference was measured. This difference is probably due to a difference of internal architecture that is also shown by comparing the specific surface area which is two times higher for yttria (19.78m^2/g) compared to zirconia (10.78m^2/g) and respectively. Such difference in architecture is also evidenced by a significant difference in crystallite sizes respectively at 79 nm for zirconia and 51 nm for yttria. Because of the porous and agglomerated structure, the micro-hardness of both powders are very low and nearly similar values within 35-40$Hv_{0.01}$ were measured for both powders.

3.2 "Splat" experiments

In previous work, particle velocities involving same LPCS CS parameters and powders were all measured to be greater than 350m/s in the central part of the jet and for spraying distances of 80mm and shorter one's [28]. For example, at 40 mm, particles velocity of 450m/s has been measured for yttria. It is therefore assumed (not measured) that an even higher velocity is obtained at 10 mm. These ranges of particle velocity and spray distance are conventional in cold spraying. However, with such small spraying distance, especially at 10mm, the bow-shock effect may affect drastically the actual impact velocity. In our work, thin films were obtained with both powders but with greater thickness and cohesion in the case of yttrium powder [28]. In this paper, it is aimed to better understand whether the bonded particles deform and fragment by examining individual particles. To this end, both powders were sprayed at atmospheric pressure (100kPa) while yttria powder was also sprayed under dynamic vacuum (3kPa). Same cold spray parameters involving 10mm and 40mm spraying distances to achieve isolated yttria and zirconia particles deposited on A2017 substrates for further observations by SEM with secondary electron detector. Representative images are given in Figure 5 for each spraying distance.

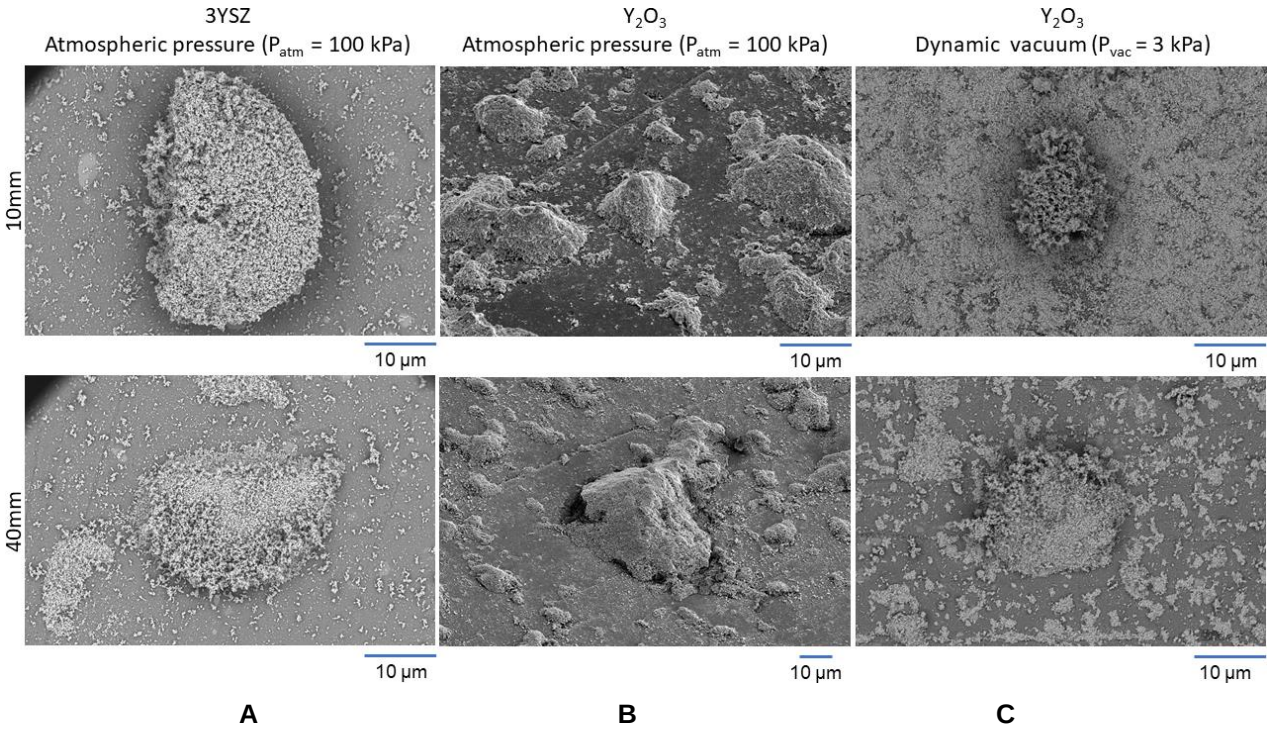

Figure 5. 3YSZ and Y_2O_3 splats for atmospheric (A and B) and Y_2O_3 for dynamic vacuum (C) conditions at 10mm or 40 mm spraying distances

According to the SEM views shown in Figure 5, splats do not have the same flattening behaviour depending on the type of powders, spraying distances and atmosphere. First, isolated zirconia particles (Figure 5, A) were generally much less present than the yttria particles (Figure 5, B) at atmospheric pressure. Despite, fewer bonded splats can be observed on the substrate for zirconia compared to yttria, it was obvious that zirconia particles were fragmented but rather undeformed, i.e., keeping the original spherical shape close to the D_{50}. From these characteristics, it can be deduced that most of the zirconia powders were in fact weakly bonded due to the effect of the bow-shock, but more likely also intensively blown by the cold spray gas stream during the process. At 40 mm, some flattening of the zirconia particles and also fragmentation, i.e small islands around a bigger one was observed. In addition, some submicrometric fragmented 3YSZ grains are also similarly dispersed and stuck on the surface for both spraying distances.

The features of yttria by LPCS at atmospheric pressure (Figure 5, B) are significantly different from those of the zirconia powder (Figure 5, A). From the observation at 10mm and 40mm, it is obvious that flattened yttria particles are more numerous especially for the shorter spraying distance. Yttria particles adhere to the substrate exhibiting a typical volcano-like shape with size roughly ranging from 5 to 30µm. The particles appear deformed and fragmented but obviously more compact than 3YSZ powder after impact. At 40 mm, similar morphologies of volcano-like splats and fragments were observed but less concentrated probably due to the widening of the stream. These splats experiments show the actual difference in spreading behaviour between both powders.

Yttria particles sprayed under dynamic vacuum (Figure 5, C) appear much more fragmented. Indeed, if some isolated splats, rather rounded may be found, it was remarkable that small grains have spread homogeneously over the substrate surface as shown at a spraying distance of 10mm. It results in a rather homogenous film than isolated splats. At 40mm, such film is less dense probably due to the widening of the jet. Such spreading behaviour under low pressure condition is therefore more govern by a micro-fragmentation process compared to an actual deformation-fragmentation evidenced at atmospheric pressure. The potential fragmentation of the powder before impact during the flight of the agglomerated powder within the supersonic stream might be questioned but also the role of the surrounding pressure on the bow-shock that could prevent very small particles grains to reach the substrate.

3.3 Flat-punch indentation and micropillar compression experiments

Load-displacement curves of three different 3YSZ grains are given in Figure 6. Grain 2 and 3 were corresponding to the monotonic loading condition while grain 1 underwent a cyclic loading with increasing depth. From Figure 6, it is obvious that the measurements on were nicely repeatable and therefore relevant with the actual behaviour of the powder. A depth of around 3µm was measured by the tip for a load of 57mN. The flat punch indentation cyclic tests reveals that the material has an elastic and some “plastic” deformation behaviour (elliptical shape is formed during the discharge). Such behaviour corresponds to the non-reversible densification under compression of the

agglomerated material. It was also observed on SEM images that the compaction was enabled mainly in the loading direction without evidence of boundary effects that could promote out-of-plane (pop-up) displacement.

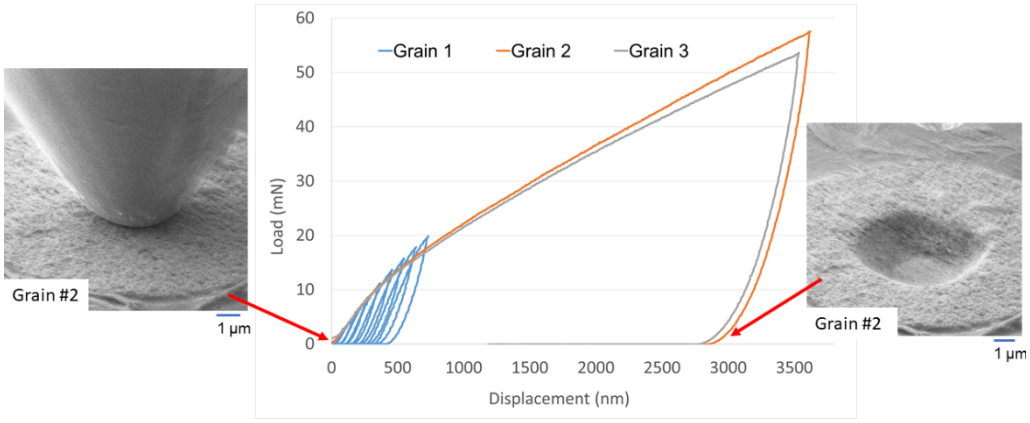

Figure 6. Load-displacement curves of flat punch indentation on three different grains

Load-displacement curves of three different 3YSZ micropillars are given in Figure 7. Pillar 2 and pillar 3 were corresponding to the monotonic loading condition while pillar 1 underwent a cyclic loading with increasing depth. From Figure 7 it was obvious that the deformation behaviour was similar up to 1mN but when increasing more, a peak load always occurred but with different maximum force respectively 1.42mN and 2.02mN for pillars 2 and 3 that corresponded to a stress of 153MPa and 210MPa respectively. It is also noticeable that this maximum peak load that was measured for pillar 3 was nearly similar to those of pillar 1 upon cyclic loading. For deeper displacement, both pillars 2 and 3 under monotonic loading exhibited the same behaviour with a final force of around 1.18mN, which corresponded to a stress of 126MPa. The first ramp of the curve recorded for each pilar was similar and showed an elastic behaviour, then plastic deformation and strain hardening appears to take place at low displacement, observed by a second ramp between 200nm and 300nm. This kind of plastic deformation (compaction) was also ascertained by the cyclic micro-compression test of pillar 1 for which ellipses were monitored during the discharge. During these first two phases, the SEM images showed a compression mainly on the top of the pillars. Just after this local plastic deformation, a decrease in force is monitored for all pillars. This part might be considered as a pseudo softening. In fact, this phenomenon reflects a damage starting with the slipping of the top of the pilar and ending by a failure of the pillar as shown in Figure 7.

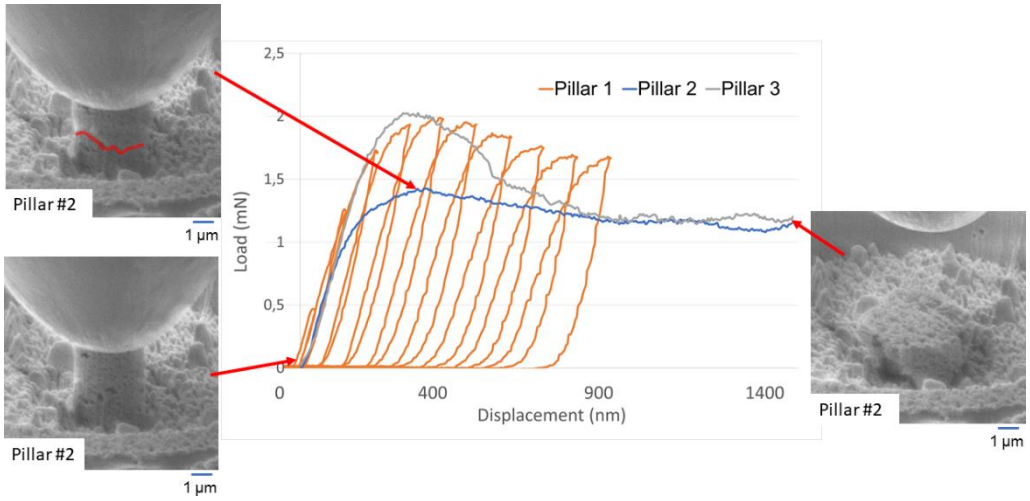

Figure 7. Load-displacement curves of flat microcompression tests on three different micropillars

3.4 Material's parameters identification of a Drucker-Prager Cap (DPC) model

An identification procedure of DPC parameters using the numerical model involving the actual pillar geometry and the surface of a grain for flat punch compression was implemented in comparison to the experimental load-displacement curves obtained with the pillar 2 and grain 2 over a period of 15sec (maximum depth 15 nm). The resulting numerical load-displacement curves obtained with the identified parameters are presented Figure 8 according DPC parameters that were determined empirically in a first approach (Table 2) and will be further numerically optimized (optimization loop).

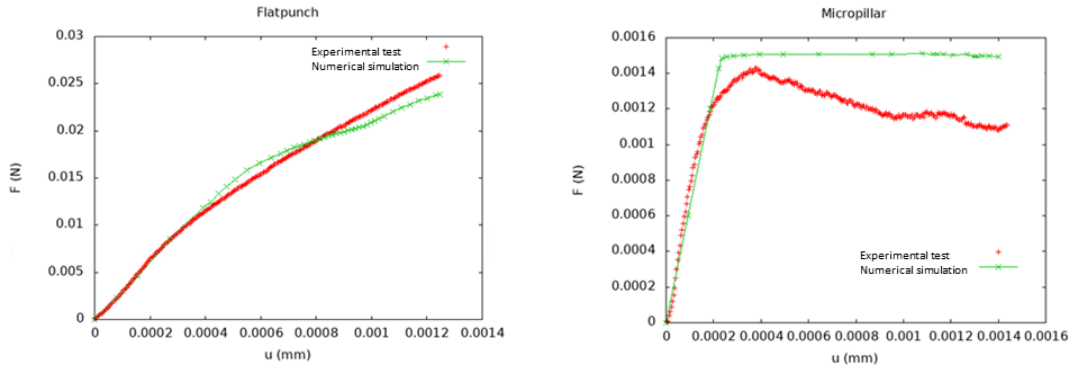

Figure 8. Experimental and numerical load-displacement curves obtained after first approach of parameters identification (left) for a flat punch experiment (right) for a micropillar experiments

Table 2. Drucker-Prager Cap initial data (first approach)

Cap plasticity						Cap hardening	
Material cohesion d	Angle of friction β	Cap eccentricity R	Initial cap yield surface position $\varepsilon_{vol}^{in}\big\vert_0$	Transition surface radius α	Flow stress ratio K	Yield stress σ_c	Volume plastic strain ε_{vol}^{pl}
						300	0
300	20	1	15	0.1	1	700	10
						1400	30

For the flat punch test, comparison of the numerical load-displacement curves with the data shows a good agreement. However, the discrepancy between 0.4 and 0.8µm displacement may be improved by a better adjustment of the DPC parameters in order to better fit with the actual displacement when the powder grain starts to compact. Normally, this adjustment would also improve the fitting of the behaviour above 0.8 µm.

Using the same material's data for the modelling of micropillar compression, a good agreement is also observed up to 0.2µm, which corresponds to the elastic and plastic part of the material behaviour. Above this value, the data of the first approach of the DPC model is not relevant and shall be improved by adjusting the Cap plasticity first and the Cap Hardening in both models. The difficulty is to simulate that the densification becomes significant only once pillar height has been reduced by more than a half, i.e., when the pillar has been significantly strained. In addition, the main limitation of the model is the fragmentation (damage model) that is not included in the DPC model.

4 Conclusions

In this work, two different agglomerated ceramic powders were analysed in order to investigate the role of their architecture on the impact behaviour during cold spray. As-atomized zirconia and yttria agglomerated powders were with different characteristics: especially in terms of porosity, specific area, crystallite sizes. Splat experiments were carried out in order to better understand the impact behaviour of bonded particles experimentally. The clear evidence of the fragmentation and deformation of the agglomerates has been observed leading to the bonding of the particle. Differences in the resulting architecture after impact are found depending on the nature of the powder but also depending on the spraying atmosphere. Yttria appears to be the powder with a better ability to "room temperature compaction impact" (RTIC). Under dynamic vacuum, highest fragmentation was enabled leading to deposition of very grains with a much more efficient and homogeneous that could explain why coatings by cold spray could be obtained more easily with this powder exhibiting a porous architecture with 50nm crystallites size leading to a large surface area of 19.8 m²/g.

In parallel, microcompression experiments on three different 3YSZ micropillars and flat punch experiments on three different grains of 3YSZ powder were carried out. These experiments demonstrated the plastic deformability of the zirconia powder that correspond to the ability to compact. In a first empirical approach, a first set of parameters in order to implement a Drucker-Prager Cap material behaviour for agglomerated powders under quasi-static compression has been developed. A numerical fitting of these parameters using an optimisation algorithm based on a Levenberg-Marquardt minimisation is on progress. If successful, such model could be then implemented in single particle compaction model using similar quasi-static loading condition.

Acknowledgments

The authors would like to thank the ANR (French Agency for Research) and all the academic and indutrial partners of the CERASOL project (ANR-19-CE08-0009): IRCER (Limoges, France), Nanoé (Ballainvilliers, France) and Medicoat France (Etupes, France), especially D. Chatelain at IRCER for his help to analyse the powders. The

following persons at MINES-PSL are gratefully acknowledged for their help for XRD analyses (C. Monteiro), TEM images and analyses (M. Sennour), cold spray experiments (J.-D. Bartout and F. Borit).

Literature

[1] A. Papyrin, *Cold spray technology*, 1. ed. Amsterdam: Elsevier, 2007.

[2] W. Li, « Solid-state additive manufacturing and repairing by cold spraying: A review », *Journal of Materials Science*, p. 18, 2018.

[3] A. Moridi, S. M. Hassani-Gangaraj, M. Guagliano, et M. Dao, « Cold spray coating: review of material systems and future perspectives », *Surface Engineering*, vol. 30, nº 6, p. 369-395, juin 2014, doi: 10.1179/1743294414Y.0000000270.

[4] H. Assadi, H. Kreye, F. Gärtner, et T. Klassen, « Cold spraying – A materials perspective », *Acta Materialia*, vol. 116, p. 382-407, sept. 2016, doi: 10.1016/j.actamat.2016.06.034.

[5] E. Kergourlay *et al.*, « First Cold Spraying of Carbonated Biomimetic Nanocrystalline Apatite on Ti6Al4V: Physical-Chemical, Microstructural, and Preliminary Mechanical Characterizations: First Cold Spraying of Carbonated Biomimetic Nanocrystalline », *Advanced Engineering Materials*, vol. 18, nº 4, p. 496-500, avr. 2016, doi: 10.1002/adem.201500409.

[6] D. Moreau, F. Borit, L. Corté, et V. Guipont, « Cold Spray Coating of Submicronic Ceramic Particles on Poly(vinyl alcohol) in Dry and Hydrogel States », *Journal of Thermal Spray Technology*, vol. 26, nº 5, p. 958-969, juin 2017, doi: 10.1007/s11666-017-0551-8.

[7] A. M. Vilardell *et al.*, « Functionalized coatings by cold spray: An in vitro study of micro- and nanocrystalline hydroxyapatite compared to porous titanium », *Materials Science and Engineering: C*, vol. 87, p. 41-49, juin 2018, doi: 10.1016/j.msec.2018.02.009.

[8] G.-J. Yang, C.-J. Li, F. Han, W.-Y. Li, et A. Ohmori, « Low temperature deposition and characterization of TiO2 photocatalytic film through cold spray », *Applied Surface Science*, vol. 254, nº 13, p. 3979-3982, avr. 2008, doi: 10.1016/j.apsusc.2007.12.016.

[9] M. Yamada, H. Isago, H. Nakano, et M. Fukumoto, « Cold Spraying of TiO2 Photocatalyst Coating With Nitrogen Process Gas », *Journal of Thermal Spray Technology*, vol. 19, nº 6, p. 1218-1223, déc. 2010, doi: 10.1007/s11666-010-9520-1.

[10] J.-O. Kliemann, H. Gutzmann, F. Gärtner, H. Hübner, C. Borchers, et T. Klassen, « Formation of Cold-Sprayed Ceramic Titanium Dioxide Layers on Metal Surfaces », *Journal of Thermal Spray Technology*, vol. 20, nº 1-2, p. 292-298, janv. 2011, doi: 10.1007/s11666-010-9563-3.

[11] L. Kong, R. Han, Y. Yang, J. Li, T. Xiong, et T. Li, « Fabrication Of Y2O3 Coatings By Cold-Spray », *AML*, vol. 10, nº 3, p. 189-192, mars 2019, doi: 10.5185/amlett.2019.2188.

[12] D. Seo, M. Sayar, et K. Ogawa, « SiO2 and MoSi2 formation on Inconel 625 surface via SiC coating deposited by cold spray », *Surface and Coatings Technology*, vol. 206, nº 11-12, p. 2851-2858, févr. 2012, doi: 10.1016/j.surfcoat.2011.12.010.

[13] M. Yamada, Y. Kandori, K. Sato, et M. Fukumoto, « Fabrication of Titanium Dioxide Photocatalyst Coatings by Cold Spray », *Journal of Solid Mechanics and Materials Engineering*, vol. 3, nº 2, p. 210-216, 2009, doi: 10.1299/jmmp.3.210.

[14] A. M. Vilardell *et al.*, « Dense nanostructured calcium phosphate coating on titanium by cold spray », *Journal of the European Ceramic Society*, vol. 37, nº 4, p. 1747-1755, avr. 2017, doi: 10.1016/j.jeurceramsoc.2016.11.040.

[15] N. T. Salim, M. Yamada, H. Nakano, et M. Fukumoto, « The Synthesis of Titanium Dioxide (TiO_2) Powder for Cold Spray Process », *IOP Conference Series: Materials Science and Engineering*, vol. 18, nº 3, p. 032019, oct. 2011, doi: 10.1088/1757-899X/18/3/032019.

[16] T. A. Rahim, K. Takahashi, M. Yamada, et M. Fukumoto, « Effect of Powder Calcination on the Cold Spray Titanium Dioxide Coating », *MATERIALS TRANSACTIONS*, vol. 57, nº 8, p. 1345-1350, 2016, doi: 10.2320/matertrans.T-M2016817.

[17] A. M. Vilardell, N. Cinca, S. Dosta, I. G. Cano, et J. M. Guilemany, « Feasibility of using low pressure cold gas spray for the spraying of thick ceramic hydroxyapatite coatings », *International Journal of Applied Ceramic Technology*, vol. 16, nº 1, p. 221-229, janv. 2019, doi: 10.1111/ijac.13088.

[18] J. Akedo, « Room Temperature Impact Consolidation (RTIC) of Fine Ceramic Powder by Aerosol Deposition Method and Applications to Microdevices », *Journal of Thermal Spray Technology*, vol. 17, nº 2, p. 181-198, juin 2008, doi: 10.1007/s11666-008-9163-7.

[19] H. Park, J. Kwon, I. Lee, et C. Lee, « Shock-induced plasticity and fragmentation phenomena during alumina deposition in the vacuum kinetic spraying process », *Scripta Materialia*, vol. 100, p. 44-47, avr. 2015, doi: 10.1016/j.scriptamat.2014.12.008.

[20] R. Moos, « An Overview of the Aerosol Deposition Method: Process Fundamentals and New Trends in Materials Applications », *J. Ceram. Sci. Tech.*, nº 03, 2015, doi: 10.4416/JCST2015-00018.

[21] J. Exner, M. Hahn, M. Schubert, D. Hanft, P. Fuierer, et R. Moos, « Powder requirements for aerosol deposition of alumina films », *Advanced Powder Technology*, vol. 26, nº 4, p. 1143-1151, juill. 2015, doi: 10.1016/j.apt.2015.05.016.

[22] B.-D. Hahn *et al.*, « Preparation and in vitro characterization of aerosol-deposited hydroxyapatite coatings with different surface roughnesses », *Applied Surface Science*, vol. 257, nº 17, p. 7792-7799, juin 2011, doi: 10.1016/j.apsusc.2011.04.031.

[23] S.-Q. Fan, G.-J. Yang, C.-J. Li, G.-J. Liu, C.-X. Li, et L.-Z. Zhang, « Characterization of Microstructure of Nano-TiO_2 Coating Deposited by Vacuum Cold Spraying », *Journal of Thermal Spray Technology*, vol. 15, nº 4, p. 513-517, déc. 2006, doi: 10.1361/105996306X146901.

[24] T. P. Mishra *et al.*, « Influence of Process Parameters on the Aerosol Deposition (AD) of Yttria-Stabilized Zirconia Particles », *J Therm Spray Tech*, vol. 30, nº 3, p. 488-502, févr. 2021, doi: 10.1007/s11666-020-01101-x.

[25] H. Ashizawa et K. Yoshida, « Investigation of fluoride layer of yttria coatings prepared by aerosol deposition method », *J. Ceram. Soc. Japan*, vol. 129, nº 1, p. 46-53, janv. 2021, doi: 10.2109/jcersj2.20174.

[26] R. Rabe *et al.*, « Observation of fracture and plastic deformation during indentation and scratching inside the scanning electron microscope », *Thin Solid Films*, vol. 469-470, p. 206-213, déc. 2004, doi: 10.1016/j.tsf.2004.08.096.

[27] ABAQUS 6.13 Theory Manual, Dassault Systemes Simulia Corp., Providence, RI, USA, 2013

[28] G. Celeste et al., “Investigation of Agglomerated and Porous Ceramic Powders Suitable for Cold Spray,” ed. F. Azarmi et al. (ITSC2021, Virtual, 2021), 139–46, https://doi.org/10.31399/asm.cp.itsc2021p0139